

# Ultrafast light scattering imaging of multi-scale transition dynamics in vanadium dioxide

Sergiy Lysenko,<sup>a)</sup> Felix Fernández, Armando Rúa, and Huimin Liu  
*Department of Physics, University of Puerto Rico, Mayaguez, Puerto Rico 00681, USA*

(Received 19 August 2013; accepted 2 October 2013; published online 18 October 2013)

Ultrafast hemispherical angle-resolved light scattering technique is applied to monitor the insulator-to-metal phase transition of highly oriented VO<sub>2</sub> crystalline films, where transition is induced by femtosecond laser pulses. This approach reveals principal differences in transient dynamics of multi-scale VO<sub>2</sub> grains for thermally and light-induced phase transformation, showing anisotropic and grain-size-dependent behavior with high resolution in space and time. Complete photoinduced transition occurs within 500 fs. However, VO<sub>2</sub> grains of different sizes show different transition rates. The highest rate is found for clusters with lower concentration of structural defects and deformations. The twinning process in VO<sub>2</sub> film is considerable for the thermally induced transition but is not detected for the ultrafast light-induced one. © 2013 AIP Publishing LLC. [<http://dx.doi.org/10.1063/1.4826074>]

## I. INTRODUCTION

Phase transition (PT) phenomena of solids are the subject of intense study in condensed matter physics.<sup>1</sup> Correlated vanadium oxide VO<sub>2</sub> is one of the semiconducting materials with complex and controversial transition dynamics.<sup>2–6</sup> The first-order structural insulator-to-metal PT of VO<sub>2</sub> can be induced in several different ways: thermally<sup>7</sup> at  $T_c = 67^\circ\text{C}$ , by an electric field and carrier injection,<sup>8,9</sup> pressure,<sup>10–14</sup> and by ultrafast laser radiation without heat transfer from the light pulse to the lattice.<sup>3,15–17</sup> Unique photorefractive properties of vanadium dioxide make this material very attractive for technological applications where light is controlled by light, such as high-speed optoelectronic units for data storage and optical signal processing, transient holograms, optical switchers, light detectors, and metamaterials.<sup>18–26</sup> A major number of these devices is based on thin polycrystalline films with different surface statistics. Small variations in surface roughness parameters affect PT properties which are very sensitive to the grain size, strain, and structural defects. Therefore knowledge about multi-scale PT dynamics in polycrystalline VO<sub>2</sub> films is of keen interest.

Much significant information about size-dependent transition properties of VO<sub>2</sub> polycrystalline films (e.g., PT rate, threshold concentration of photoexcited carriers, structural deformations, coexistence of different phases, critical size of nucleus, PT temperature, hysteresis, etc.) still remains unknown owing to technical difficulties to study fast kinetics with high spatial resolution. In this connection emerging state-of-the-art ultrafast 4D electron microscopy,<sup>27,28</sup> X-ray and electron diffraction techniques<sup>4,29–34</sup> receive special attention since the wave diffraction arises from inhomogeneity in the material and can provide statistical information about structural dynamics with superior resolution in space and time. However, these methods have relatively low sensitivity to monitor electronic excitations. In contrast, optical

methods are highly sensitive to fluctuations of electron charge density as well as to lattice structure, stoichiometry, size, and shape of small particles. Ultrafast optical diffraction provides a very promising approach to obtain information about correlations between photoexcited state dynamics, grain size, and structural disorder of stochastic surfaces. Particularly, angle-resolved light scattering technique combined with femtosecond pump-probe spectroscopy can shed light upon statistical transient processes in VO<sub>2</sub> and separate charge and lattice dynamics in particles of different size.

In the present work we use hemispherical elastic light scattering to study matter far from equilibrium. Angle-resolved scattering nondestructively reveals anisotropic grain-size-dependent PT dynamics in VO<sub>2</sub> films, showing significant differences between thermally- and light-induced processes on the mesoscopic spatial scale. It is shown that the transition rate in light-induced PT is highest within clusters with lower concentration of structural defects and deformations. The evolution of anisotropic scattering pattern suggests a complex non-twinning transition within 500 fs. Thermally induced PT is essentially different and accompanied by the film twinning and deformations due to long-range interatomic interactions.

## II. EXPERIMENT

Polycrystalline 30-nm-thick VO<sub>2</sub> films were grown by pulsed laser deposition technique on R-cut (012) Al<sub>2</sub>O<sub>3</sub> (sapphire) single crystal substrates. These substrates were chosen to synthesize VO<sub>2</sub> films with highly oriented close-packed crystallites with a relatively low concentration of structural defects.<sup>35,36</sup> An excimer KrF laser with 248 nm wavelength, 20-ns pulses focused to  $\sim 4\text{ J/cm}^2$  fluence onto a rotating metallic vanadium target was used in the laser ablation process. VO<sub>2</sub> films were grown in an oxygen and argon atmosphere, with O<sub>2</sub> and Ar flow rates of 20 and 5 std. cm<sup>3</sup>/min, respectively, and total chamber pressure of 30 mTorr. Substrate temperature was maintained at 550 °C during deposition.

<sup>a)</sup>Electronic mail: sergiy.lysenko@upr.edu

A Bruker D8 Discover X-ray diffractometer equipped with a  $\frac{1}{4}$ -circle Eulerian cradle goniometer was used to obtain information about phase composition and crystallographic orientation of the VO<sub>2</sub> films grown on the sapphire substrates. The surface geometry was probed by atomic-force-microscopy (AFM, Park Scientific Instruments, Autoprobe CP).

Angle-resolved elastic light scattering was recorded with a scatterometer shown in Fig. 1(a). This setup was built in reflection geometry for hemispherical scattering measurements with femtosecond resolution. Experiments were conducted in two different regimes: (i) ultrafast time-resolved pump-probe scattering measurements and (ii) stationary measurements without use of high-intensity pump laser pulses for nonlinear interaction with the sample. To realize ultrafast light-induced PT a Spectra-Physics Ti:Sapphire laser system was used as a source of 130 fs light pulses with 100 Hz repetition rate. Collinear pump (wavelengths  $\lambda_p = 800$  nm, 0.7 mm diameter Gaussian spot) and frequency-doubled probe (wavelengths  $\lambda_{pr} = 400$  nm,  $\sim 100 \mu\text{m}$  spot size) pulses are overlapped in the sample at normal incidence. Both  $\lambda_p$  and  $\lambda_{pr}$  wavelengths are within fundamental absorption region of VO<sub>2</sub>. However, there is an advantage using a shorter wavelength as a probe. Thus, the information obtained from scattering indicatrix at  $\lambda_{pr} = 400$  nm covers broader range of surface spatial frequencies. Also, scattering at  $\lambda_{pr} = 400$  nm is much stronger as compared to  $\lambda_p = 800$  nm, since the scattering intensity is proportional to  $\lambda^{-4}$ . Moreover, using a blue filter in two wavelengths experiment it was easy to transmit only probe light scattering into the detector and eliminate undesirable scattering of pump beam. Structural PT in VO<sub>2</sub> film was produced by optical pump with 10 mJ/cm<sup>2</sup> fluence at room temperature. At this excitation level the nonlinear optical response of VO<sub>2</sub> represents mainly PT dynamics.<sup>29</sup> The probe light intensity was substantially reduced by a neutral density filter in order to prevent nonlinear interaction with the sample. Time delay between probe and pump pulses was controlled by an

optomechanical delay line. Scattering of probe light was collected by a custom-built elliptical metallic mirror with 20-cm diameter and recorded by 16-bit charge-coupled-device (CCD) camera as a function of time delay between pump and probe pulses or as a function of sample temperature (Fig. 1). Integrated light scattering intensity over the hemisphere was also measured by an amplified silicon detector conjugated with a gated data processor.

Stationary scattering measurements were performed to study thermally induced PT process. A 2 mW continuous wave He-Ne laser with  $\lambda_{pr} = 632.8$  nm was used as a probe. The PT was produced with a Peltier heater mounted on the sample holder.

In this study the scattering indicatrices were measured and mapped by Bidirectional-Scatter-Distribution-Function (BSDF) versus polar  $\theta$  and azimuthal  $\varphi$  angles as well as a function of spatial frequency  $f$ . This scattering function depends on directions of incident and scattered light and is the surface brightness divided by surface irradiance, and as defined by<sup>37</sup>

$$BSDF(\theta, \varphi) = \frac{1}{I_0} \left( \frac{dI_{scat}(\theta, \varphi)}{d\Omega} \right) \frac{1}{\cos \theta}, \quad (1)$$

where  $dI_{scat}(\theta, \varphi)$  is the scattered light intensity within a solid angle  $d\Omega$ , and  $I_0$  is the incident light intensity.

### III. RESULTS

#### A. Structure of VO<sub>2</sub> thin films

X-ray diffraction (XRD) data show that the films are single monoclinic M<sub>1</sub> phase at room temperature, with (100) planes parallel to the substrate surface, as shown by the (200) VO<sub>2</sub> diffraction peak at  $2\theta = 37.1^\circ$  [Fig. 2(a)]. The much weaker (400) peak (not shown in this scan) was also observed. Hence, the (100) VO<sub>2</sub> plane is parallel to the (012) plane of Al<sub>2</sub>O<sub>3</sub> substrate. Peaks at  $2\theta = 25.6^\circ$  and  $2\theta = 52.6^\circ$  in this  $\theta - 2\theta$  scan are due to (012) and (024) Bragg reflections of the CuK <sub>$\alpha$</sub>  X-ray line on the Al<sub>2</sub>O<sub>3</sub> substrate lattice. Sharp peaks close to the substrate (012) and (024) peaks are ghost reflections of the same peaks, due to the Cu K <sub>$\beta$</sub>  line and the tungsten L <sub>$\alpha$</sub>  line owing to impurity from the filament of the x-ray tube deposited on its copper target.

Preferred in-plane orientation of VO<sub>2</sub> crystallites on the sapphire substrate was determined by azimuthal XRD measurements. The film (002) reflection was found at the expected goniometer inclination ( $\chi = 57.40^\circ$ ) for the interplanar angle between the (100) and (001) planes of VO<sub>2</sub>. One single reflection was found for the full azimuthal scan, as expected from the crystal geometry [Fig. 2(b)]. The azimuth angular position for this peak nearly coincides with that of the substrate (006) reflection. The latter was obtained at a goniometer inclination  $\chi = 57.61^\circ$ , corresponding to the interplanar angle between the substrate (001) planes and its (012) surface plane and is also observed just once in the scan, as appropriate for the single-crystal sapphire symmetry. This indicates that in fact the film [010] direction is parallel to the substrate [100] direction. This and additional

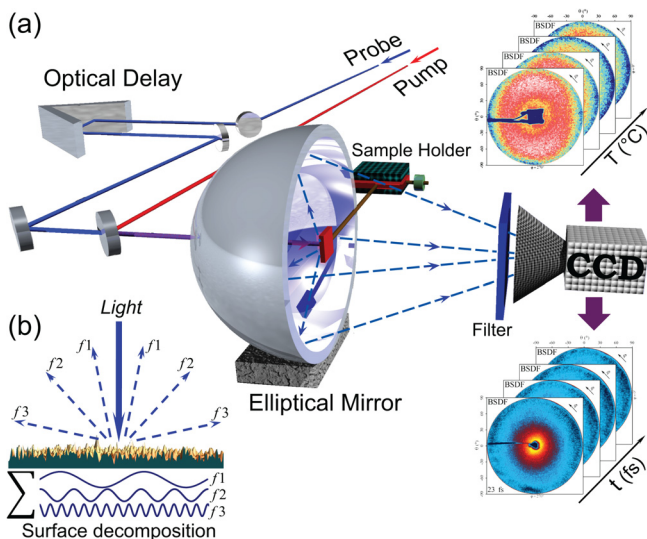


FIG. 1. Experimental geometry and imaging of surface light scattering. (a) Schematic layout of ultrafast scatterometer. (b) Sketch of light scattering by Fourier components of surface roughness.

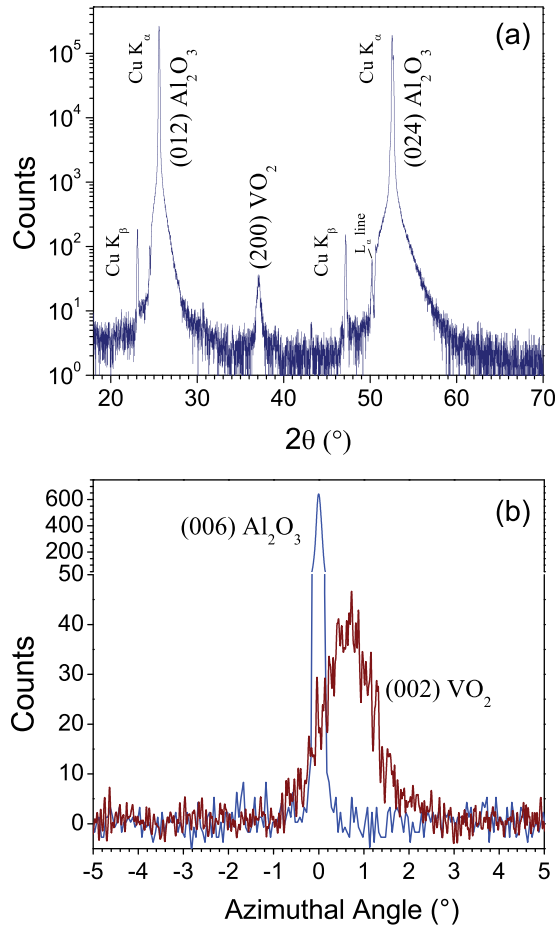


FIG. 2. X-ray diffraction from VO<sub>2</sub> film and R-cut Al<sub>2</sub>O<sub>3</sub> substrate. (a)  $\theta$ - $2\theta$  XRD geometry. (b) Diffraction signal versus azimuthal orientation of the sample for two different goniometer tilt angles  $\chi$ .

azimuthal scans showed that the film was epitaxial with respect to the sapphire R-cut substrate lattice, with  $c_m$  and  $b_m$  crystallographic directions in the surface plane.

AFM surface analysis shows dispersion of largest VO<sub>2</sub> crystallites within 200-350 nm (Fig. 3). This lateral size cannot be resolved by the scattering setup. However clusters formed by two crystallites are detectable in scattering measurements and they show specific transient optical properties, as will be shown below. Arbitrary cross-sections of AFM images show that the characteristic size of these clusters is

0.55–0.63  $\mu\text{m}$  ( $f \approx 1.6$ – $1.8 \mu\text{m}^{-1}$ , in terms of spatial frequencies). While the PLD process can also produce droplets, very few of these were observed by AFM or optical microscope. The typical size of droplets is several microns. Therefore their contribution to light scattering indicatrix occurs at low spatial frequencies, within few degrees near  $\theta = 0^\circ$ . However in scattering measurements this angular range was out of observation.

## B. Elastic light scattering

Angle-resolved scattering was measured within hemisphere and mapped as a function of polar  $\theta$  and azimuthal  $\varphi$  angles and also versus the spatial frequency of surface relief Fourier decomposition.<sup>38</sup> The surface relief can be represented as a superposition of sinusoidal diffraction gratings with different periods  $d$ , amplitudes, phases, and orientations, where each grating diffracts light only in two symmetric directions in space [Fig. 1(b)]. Light scattering intensity increases with fluctuations of the dielectric constant  $\epsilon$  and therefore is used to monitor structural disorder. Thus, collecting the time- and angle-resolved scattering over a hemisphere we obtain statistical information about grain sizes and orientation, local morphology, and also the structural transformation of VO<sub>2</sub> films with temporal and spatial resolution. The scattering technique allows reconstruction of the surface power-spectral-density function PSD( $f$ ), which precisely represents surface irregularities as a function of spatial frequency  $f = 1/d = \sin\theta/\lambda_{pr}$ .<sup>37,39,40</sup> However, rigorous calculation of PSD( $f$ ) for the VO<sub>2</sub> transition process is problematic since PT is accompanied with considerable changes of optical constants. Nevertheless, statistical information about surface structure and its evolution can be obtained from analysis of the BSDF commonly used in scattering measurements. This function can be obtained experimentally, and the relation between BSDF and PSD is defined as<sup>37</sup>

$$BSDF(\vec{f}) = \frac{16\pi^2}{\lambda_{pr}^4} Q \cos\theta_i \cos\theta_s PSD(\vec{f}), \quad (2)$$

where  $\theta_i$  and  $\theta_s$  are incident and scattering angles, respectively,  $Q$  is an optical factor which depends on material dielectric constants and light polarization. Scattering experiments in most cases show one-to-one BSDF/PSD relationship

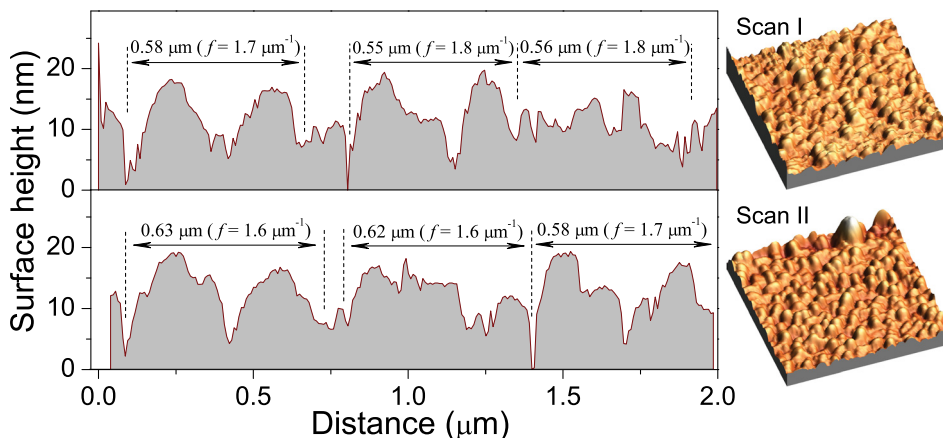


FIG. 3. Topography of VO<sub>2</sub> film surface. Right panel: Surface topography for two different AFM  $2 \times 2 \mu\text{m}$  scans. Left panel: arbitrary cross-section of each scan.

in the smooth-surface limit.<sup>37</sup> Therefore, analysis of BSDF data conveys reliable information about size-dependent distribution of surface inhomogeneities in the sample.

Since the light scattering depends both on optical constants and inhomogeneity of the material, the scattering from thin VO<sub>2</sub> film and from bulk is slightly different. The surface structure and optical constants of thin films strongly depend on substrate type, substrate roughness, film thickness, and defects. The angular distribution of scattered light is a complex function of all these parameters.<sup>37,39</sup> In the present study, 30-nm-thick VO<sub>2</sub> film consists of highly oriented crystallites due to epitaxial growth on single crystal Al<sub>2</sub>O<sub>3</sub> substrate, as confirmed by XRD. Since surface irregularities are aligned along preferential directions, the light scattering has azimuthal anisotropy, as will be shown below. A lower degree of structural anisotropy was found for thicker PLD films, and light scattering by such films will not be discussed here.

### 1. Light-induced phase transition

In order to induce the PT uniformly through the whole film, the films were prepared with 30 nm thickness, which is significantly less than the characteristic penetration depth of light ( $\sim 150$  nm in the insulating phase for  $\lambda_p = 800$  nm pump). The angular distribution of scattered light was mapped by BSDF( $\theta, \varphi$ ). As shown before,<sup>41,42</sup> light

scattering decreases during the insulator-to-metal PT of VO<sub>2</sub>. The rapid drop of the scattering signal in Figs. 4(a) and 4(b) indicates that the transition occurs within 500 fs. This behaviour is similar to the typical transient evolution of reflection and transmission<sup>29,43</sup> due to structural PT in the film. However, the BSDF indicatrix contains additional information about the ultrafast optical dynamics of individual spatial structures with different azimuthal orientations and spatial frequencies.

The VO<sub>2</sub> films on crystalline Al<sub>2</sub>O<sub>3</sub> substrates are formed by highly oriented close-packed VO<sub>2</sub> crystallites.<sup>35,36</sup> X-ray diffraction analysis has shown that the  $c_m$  and  $b_m$  crystallographic directions of monoclinic VO<sub>2</sub> crystallites are parallel to the surface plane and are epitaxially oriented with the substrate (Fig. 2). Such lateral orientation of the VO<sub>2</sub> lattice results in preferred orientation of crystallites and in a slight anisotropy of the BSDF indicatrix, observable in Fig. 4(a). Moreover, mapping of the scattering data as a relative change of measured signal  $\Delta\text{BSDF}(t)/\text{BSDF}(0)$  [Fig. 4(c)], where  $\Delta\text{BSDF}(t) = \text{BSDF}(t) - \text{BSDF}(0)$ , gives new information about multi-scale PT dynamics. This reveals explicit *transient anisotropy* caused by spatial ordering of VO<sub>2</sub> crystallites [Fig. 4(c)]. Initially the PT starts as a uniform isotropic transition. However, some scattering anisotropy appears after 200 fs and becomes clearly distinguishable at  $\sim 260$  fs. With increasing delay time the indicatrix shows a fairly sharp square-like pattern oriented along  $c_m$  and  $b_m$

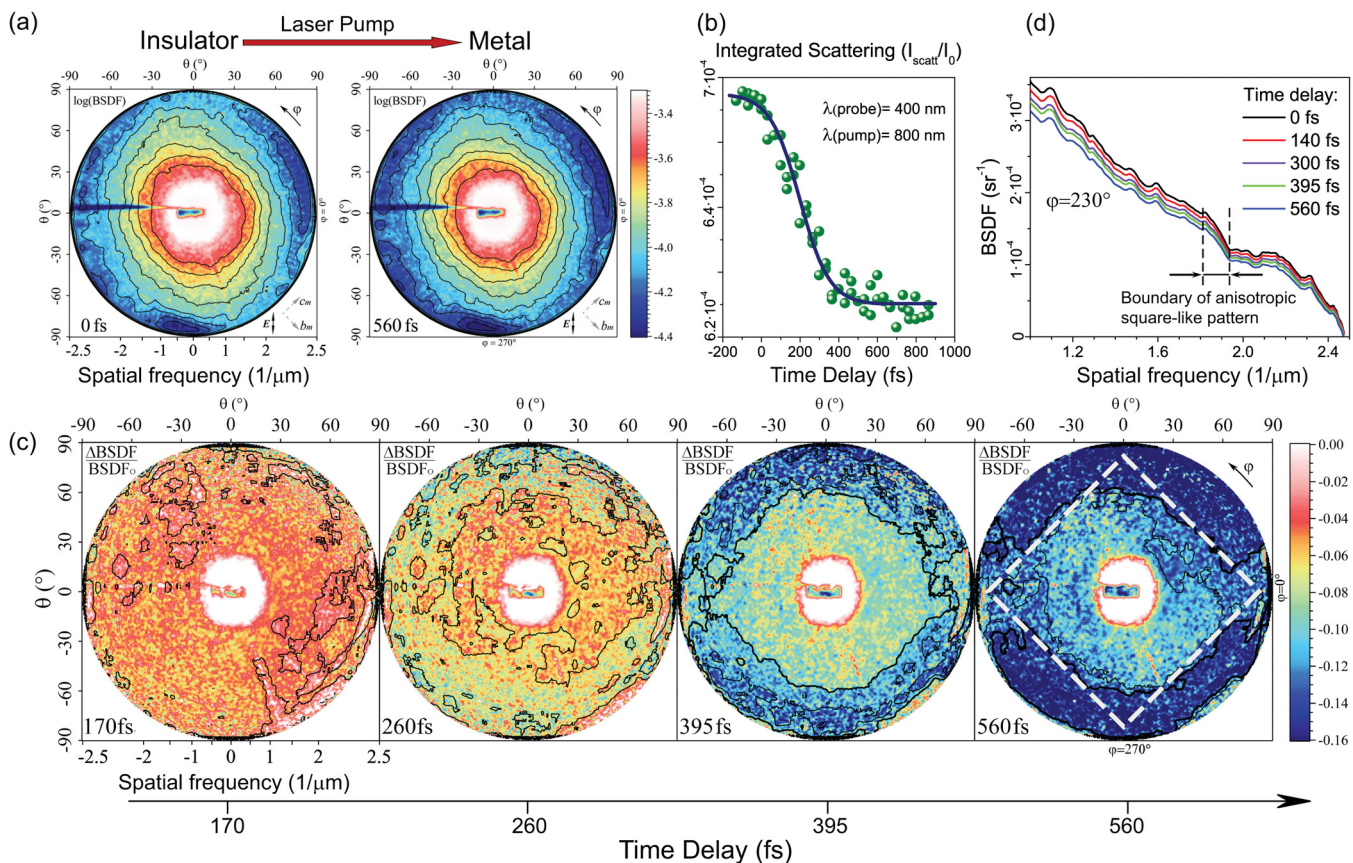


FIG. 4. Light scattering as a function of pump-probe pulse delay upon light-induced insulator-to-metal phase transition. (a) Scattering indicatrices for insulating and metallic phases. (b) Scattering light intensity  $I_{\text{scatt}}$  integrated over hemisphere normalized to the incident intensity  $I_0$ . (c) Corresponding dynamics of  $\Delta\text{BSDF}(t)/\text{BSDF}(0)$ . Dashed isophotes at  $t = 560$  fs outline a square-like pattern. (d) Cross-section of BSDF indicatrix versus spatial frequency (enhanced online). [URL: <http://dx.doi.org/10.1063/1.4826074.1>]

crystallographic directions of the VO<sub>2</sub> sample. This pattern is outlined by isophotes within polar angle  $\theta = 50\text{--}65^\circ$  for  $t = 560$  fs.

Cross-sections of scattering indicatrices at any azimuthal angle show similar transient behavior of BSDF( $f$ ): PT results in monotonic decrease of BSDF( $f$ ) for all spatial frequencies [Fig. 4(d)].

## 2. Thermally induced transition

Scattering indicatrices for thermal transition are shown in Fig. 5(a). They are obtained for another area of the sample and for different wavelength and, therefore, have slightly different pattern. Nevertheless, they also show a preferred azimuthal orientation due to crystallographic orientation of VO<sub>2</sub> film on Al<sub>2</sub>O<sub>3</sub> substrate. Within the tested area, VO<sub>2</sub> crystallites have formed a slight periodical structure with period  $d \approx 1 \mu\text{m}$ , giving symmetrical diffraction peaks  $A'$ - $A$  at  $\varphi = 150^\circ, 330^\circ$ . Cross-sections of the indicatrix at different temperatures for insulator-to-metal PT are shown in Fig. 5(b) at  $\varphi = 270^\circ$ , and in Fig. 5(c) for complete cycle of insulator-metal-insulator PT at  $\varphi = 330^\circ$ . The scattering pattern undergoes significant change upon thermally induced transition for each azimuthal direction. Fig. 5(b) shows irregularities of BSDF( $f$ ) marked by arrows which emerge during PT, and Fig. 5(c) shows a shift of scattering peaks  $A$ ,  $B$ , and  $C$  to higher spatial frequencies.

The PT also alters integrated scattering intensity within the hemisphere, showing hysteric behavior [Fig. 5(d)]. As temperature increases, the phase changes from insulating to metallic, and scattering signal drops in similar way as in the

light-induced PT. However, structural disorder of the film near the PT point results in pronounced increase of the signal [dashed portion in Fig. 5(d)]. The same behavior is observed for metal-to-insulator recovery process.

## IV. DISCUSSION

Recent study of ultrafast light-induced PT by Wall *et al.*<sup>3,44</sup> has shown that the coherent oscillations of V-V dimers vanish on  $\sim 200$  fs time scale after sufficiently high laser excitation. However the complete insulator-to-metal transition lasts much longer, where the entire relaxation process strongly depends on excitation level. Ultrafast electron diffraction<sup>4</sup> shows a stepwise atomic motions within the unit cell with characteristic times of 370 fs and 9.2 ps. Our results support these findings and suggest a stepwise PT dynamics on subpicosecond scale in thin film at sufficient optical pump. Since VO<sub>2</sub> films used in this study are highly oriented in the surface plane, the anisotropy of light scattering is related to crystallographic orientation of the film. The transient anisotropy appears in the scattering indicatrix after 200 fs [Fig. 4(c)] and is strong evidence of structural transformation of the film from monoclinic to tetragonal metallic phase. However, during the first 200 fs the scattering signal drops without showing anisotropy. This indicates that before and after  $\sim 200$  fs the pathway of structural transformation is different and can be related to stepwise atomic motion, as observed in Ref. 4. It is also likely that the 130 fs laser excitation produces uniform metallization of VO<sub>2</sub> due to formation of a photoexcited dense electron-hole plasma, and certainly results in renormalization of the VO<sub>2</sub> band structure

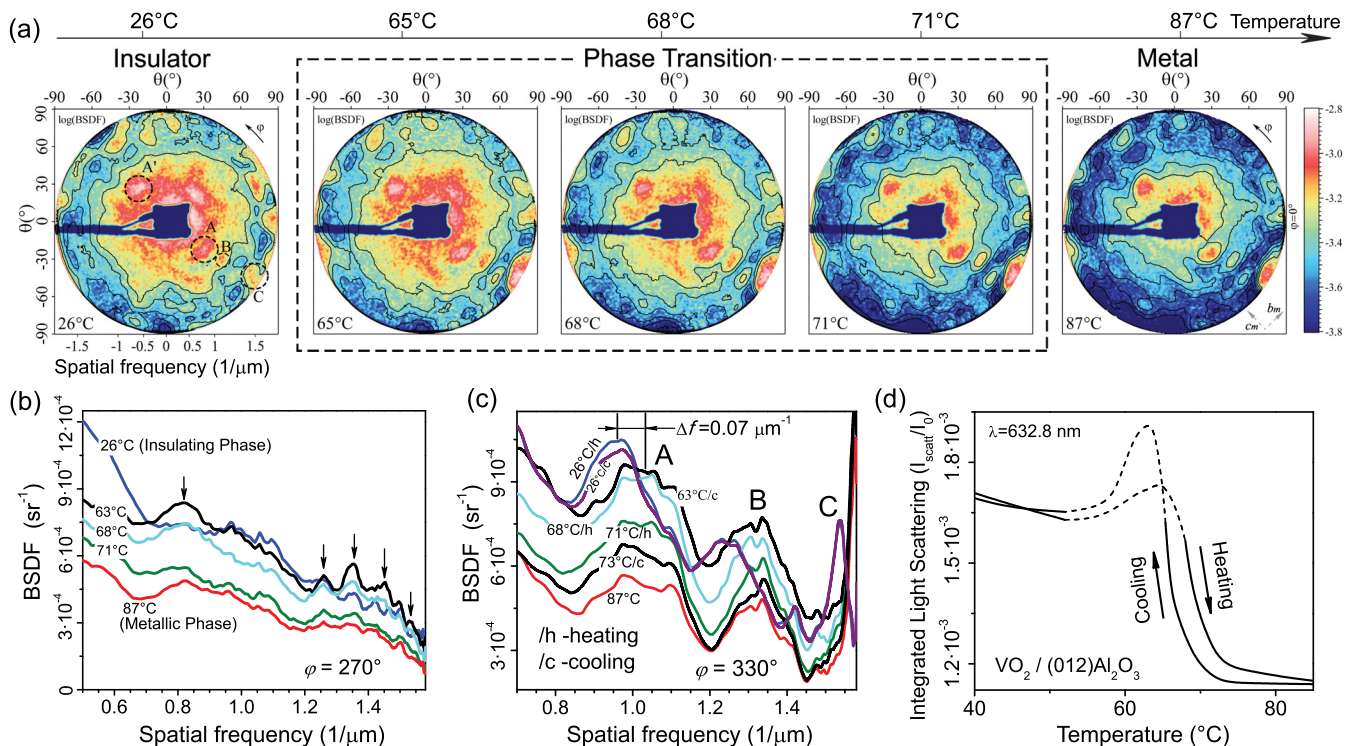


FIG. 5. Thermally induced transition. (a) Scattering indicatrices as a function of sample temperature across insulator-to-metal transition. (b) Spatial frequency dependence of BSDF( $f$ ) measured at  $\varphi = 270^\circ$  and (c) at  $\varphi = 330^\circ$ . Letters  $A$ ,  $B$ , and  $C$  indicate the same peaks as in Fig. 5(a) at  $T = 26^\circ\text{C}$ . (d) Hysteric evolution of integrated light scattering intensity over hemisphere. Dashed portion corresponds to disordered multiphase VO<sub>2</sub> structure (enhanced online). [URL: <http://dx.doi.org/10.1063/1.4826074.2>]

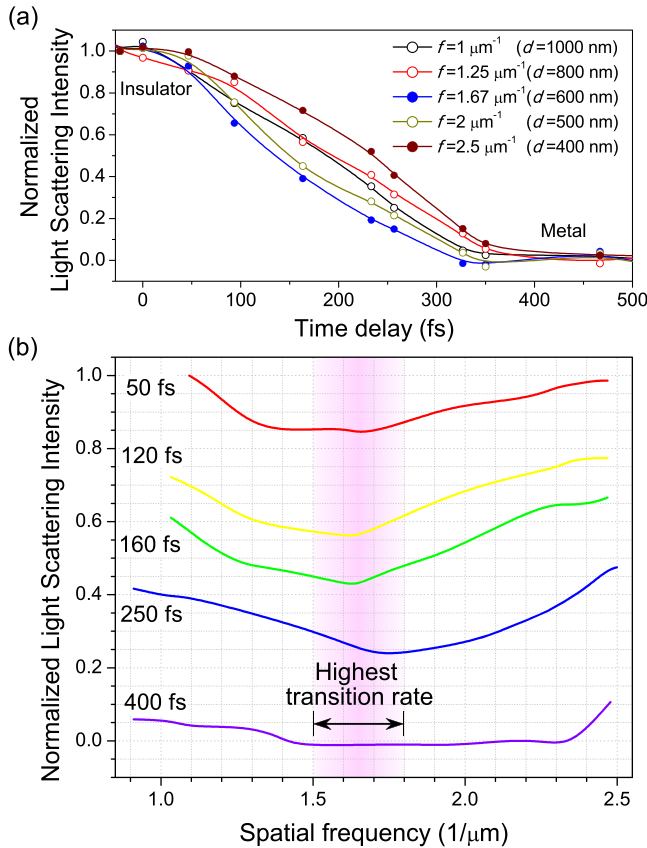


FIG. 6. Size-dependent light-induced transition dynamics. (a) Normalized light scattering signal  $\text{BSDL}(t)$ . (b) Light scattering signal versus spatial frequency of surface relief decomposition at different time delays.

due to strong free-carrier screening effects,<sup>45,46</sup> significantly affecting optical properties at the initial stage of PT.

The final indicatrix at  $t = 560$  fs in Fig. 4(c) shows that the relative change in scattering intensity is larger for smaller grains (large  $\theta$ , higher spatial frequencies). This can originate from structural defects (e.g., dislocations, oxygen vacancies, etc.), especially from local tensions in the smallest grains.<sup>47</sup> Thus, during deposition, the  $\text{VO}_2$  film was synthesized with relatively low elastic strain in its metallic tetragonal phase. However when the film is cooled down to room temperature at the end of deposition,  $\text{VO}_2$  lattice transforms to the insulating monoclinic phase, and crystallites undergo increased elastic strain. The random field of local tensions produces fluctuations of the dielectric constant  $\epsilon$ . The light-induced structural transformation back to metallic state thus reduces local tensions and fluctuations of  $\epsilon$ . We note that such behavior was directly observed for defect luminescence in Ref. 48. This occurs more markedly among smaller grains and, as a result, reduces the light scattering more strongly at higher spatial frequencies, as shown in Fig. 4(c).

The size-dependent rate of PT is one of the poorly explored problems in the physics of solid. Ultrafast angle-resolved scattering technique provides information about PT rate statistically from the cross-section of the scattering indicatrix [Fig. 4(d)]. Figure 6 shows normalized scattering light intensities measured at azimuthal angle  $\varphi = 230^\circ$ . The maximal signal here corresponds to scattering by insulating  $\text{VO}_2$ ,

and zero level corresponds to scattering by the metallic phase. These data allow comparing the PT rate for grains of different size: the difference in the rate appears as a different temporal evolution of the scattering intensity at various spatial frequencies. Since the signal drops faster at  $f \approx 1.5\text{--}1.8 \mu\text{m}^{-1}$ , structures with these spatial frequencies undergo the fastest transition. It is interesting to note that the spatial frequency  $f = 1.8 \mu\text{m}^{-1}$  for the fastest transition is at the boundary of the square-like pattern outlined by isophotes at  $t = 560$  fs [Fig. 4(c)], and the cross-section of the BSDL indicatrix [Fig. 4(d)] has an abrupt change above  $f = 1.8 \mu\text{m}^{-1}$ . Comparison of atomic force microscopy data (Fig. 3) with Fig. 4(d) and Fig. 6 shows that the spatial frequencies of highest PT rate within  $f = 1.6\text{--}1.8 \mu\text{m}^{-1}$  ( $d = 550\text{--}630 \text{ nm}$ ) correspond to the characteristic surface clusters, formed by two large  $\text{VO}_2$  crystallites. Therefore, such clusters are considered as a base unit of the surface with highest transition rate. It is likely that these clusters in the polycrystalline film are similar to domains in a single crystal: they are formed with minimal and uniform structural deformations so as to minimise elastic energy. Moreover, the concentration of structural defects within such clusters is expected to be relatively low, since they are formed by the largest (200–350 nm)  $\text{VO}_2$  crystallites with higher crystalline perfection.<sup>49</sup> In this context the highest PT rate can be assigned to the  $\text{VO}_2$  clusters with lower structural deformations and concentration of defects.

The role of structural defects in ultrafast light-induced PT should be significant.<sup>36</sup> Thus, trapping of photoexcited electrons on defect levels reduces the number of photoexcited free carriers involved in I-M PT process. Structural defects also change the charge-transfer properties of  $\text{VO}_2$ . The charge-transfer can be a possible mechanism for the ultrafast subpicosecond PT,<sup>36</sup> where the disorder of  $\text{VO}_2$  film will increase characteristic transition time.

The angle-resolved scattering technique shows a significant difference in structural dynamics between light-induced and thermally induced PTs. Statistical information about thermal transition was obtained from BSDL indicatrices in Fig. 5. Here the PT results in emergence and decay of specific peaks in the scattering indicatrix [marked by arrows in Fig. 5(b)] associated with elastic deformations, twinning, and coexistence of insulating and metallic phases in the film.<sup>5,32</sup> Fluctuations of these peaks are pronounced near the PT point  $T_c = 67^\circ\text{C}$  but also occur at temperatures below and above this point owing to significant change of the film strain energy. The surface topography is strictly defined by the strain energy at the boundary between single-crystal  $\text{Al}_2\text{O}_3$  substrate and  $\text{VO}_2$  film. The PT alters this energy and results in structural modification of the surface. Thus, the indicatrix cross-section along the periodical structure formed by  $\text{VO}_2$  crystallites [Fig. 5(c)] shows a reversible change  $\Delta f = 0.07 \mu\text{m}^{-1}$  of its spatial frequency at a temperature above  $26^\circ\text{C}$ , manifesting a shrinking of this structure due to elastic deformation and twinning process. It is also possible that some diffraction peaks appear due to transition into  $\text{M}_2$  phase within strained  $\text{VO}_2$  domains.<sup>12–14,50</sup>

The light scattering near PT point is strongly related to structural disorder of  $\text{VO}_2$  polycrystalline film owing to

fluctuations of PT order parameter  $\eta$ . Here the role of internal strains and structural defects is expected to be dominant. Thus, strains and defects alter the order parameter  $\eta$  in their close vicinity.<sup>51</sup> The fluctuations of  $\eta$  grow near the critical point, resulting in coexistence of  $M_1$  and R and sometimes  $M_2$  phases of  $\text{VO}_2$ . In total integrated scattering this appears as a sharp rise of the signal [dashed portion in Fig. 5(d)]. It is remarkable that such scattering feature was not detected for light-induced transition [Fig. 4(b)], indicating a different pathway of PT dynamics. Comparison of BSDF( $f$ ) for light- and thermally induced PTs supports this assumption.

In the light-induced transition the evolution of BSDF( $f$ ) is monotonic, without significant change in slope and shape [Fig. 4(d)], while the thermally induced one is accompanied by significant distortion of BSDF( $f$ ) due to film twinning, elastic deformations and coexistence of different phases [Figs. 5(b) and 5(c)]. In the light-induced PT the uniform decrease of BSDF( $f$ ) versus time suggests no twinning or change in the surface geometry: the insulating phase is switching to the metallic one coherently through all spatial frequencies within 500 fs. These results indicate that the thermal PT is accompanied with long-range interatomic interactions due to temperature dependent strains and shear deformations, while in the light-induced transition only local, short-range interactions should be taken into account.

## V. CONCLUSIONS

In conclusion, the time-resolved imaging of hemispherical light scattering shows transient anisotropy due to structural transformation of highly oriented  $\text{VO}_2$  film. Scattering anisotropy is observed only after 200 fs while the film metallization occurs continuously within 500 fs. Such a behavior suggests a stepwise structural transformation of the film. Comparison of scattering indicatrices obtained for different PT regimes shows essential difference between light- and thermally induced transition dynamics.  $\text{VO}_2$  scattering during thermal PT reveals significant film twinning and phase coexistence near PT point. The film twinning is accompanied by long-range interatomic interactions and occurs mainly due to presence of structural defects and elastic strains. In the case of light-induced PT the film twinning was not detected. This indicates that the short-range interatomic interactions play dominant role in this transition. It is believed that the ultrafast twinning could occur within local areas of structural defects. However, if this takes place, the overall contribution of twinned domains in scattering signal is rather small for high purity  $\text{VO}_2$  film. Upon light-induced transition different crystallites transform synchronously to the metallic phase. Nevertheless, the PT rate differs for grains of different size. The fastest transition occurs within surface structures with spatial frequencies of  $f \approx 1.5\text{--}1.8 \mu\text{m}^{-1}$ . Comparison of AFM and scattering data shows that these structures are presumably formed by two crystallites with lower concentration of defects and deformations. The size  $\text{VO}_2$  particles and concentration of defects both affect the PT rate. However for thin polycrystalline films with relatively large crystallites, with an average lateral size of about 300 nm, the influence of structural defects on PT rate is expecting to be dominant.

## ACKNOWLEDGMENTS

The authors gratefully acknowledge helpful discussions with Valeriy Sterligov and his contribution in production of the elliptical mirror. This work was supported by UPRM College of Arts and Sciences and NSF-EPSCoR office.

- <sup>1</sup>M. Imada, A. Fujimori, and Y. Tokura, *Rev. Mod. Phys.* **70**, 1039 (1998).
- <sup>2</sup>A. Cavalleri, *Science* **318**, 755 (2007).
- <sup>3</sup>S. Wall, D. Wegkamp, L. Foglia, K. Appavoo, J. Nag, R. F. Haglund, Jr., J. Stähler, and M. Wolf, *Nat. Commun.* **3**, 721 (2012).
- <sup>4</sup>P. Baum, D.-S. Yang, and A. H. Zewail, *Science* **318**, 788 (2007).
- <sup>5</sup>M. M. Qazilbash, M. Brehm, B.-G. Chae, P.-C. Ho, G. O. Andreev, B.-J. Kim, S. J. Yun, A. V. Balatsky, M. B. Maple, F. Keilmann, H.-T. Kim, and D. N. Basov, *Science* **318**, 1750 (2007).
- <sup>6</sup>V. Eyert, *Phys. Rev. Lett.* **107**, 016401 (2011).
- <sup>7</sup>F. J. Morin, *Phys. Rev. Lett.* **3**, 34 (1959).
- <sup>8</sup>G. Stefanovich, A. Pergament, and D. Stefanovich, *J. Phys.: Condens. Matter* **12**, 8837 (2000).
- <sup>9</sup>H.-T. Kim, B.-J. Kim, Y. W. Lee, B.-G. Chae, and S. J. Yun, *Physica B* **403**, 1434 (2008).
- <sup>10</sup>J. Wu, Q. Gu, B. S. Guiton, N. de Leon, O. Lian, and H. Park, *Nano Lett.* **6**, 2313 (2006).
- <sup>11</sup>J. Cao, E. Ertekin, V. Srinivasan, W. Fan, S. Huang, H. Zheng, J. W. L. Yim, D. R. Khanal, D. F. Ogletree, J. C. Grossman, and J. Wu, *Nat. Nanotechnol.* **4**, 732 (2009).
- <sup>12</sup>A. Tselev, E. Strelcov, I. A. Luk'yanchuk, J. D. Budai, J. Z. Tischler, I. N. Ivanov, K. Jones, R. Proksch, S. V. Kalinin, and A. Kolmakov, *Nano Lett.* **10**, 2003 (2010).
- <sup>13</sup>A. Tselev, I. A. Luk'yanchuk, I. N. Ivanov, J. D. Budai, J. Z. Tischler, E. Strelcov, A. Kolmakov, and S. V. Kalinin, *Nano Lett.* **10**, 4409 (2010).
- <sup>14</sup>J. H. Park, J. M. Coy, T. S. Kasirga, C. Huang, Z. Fei, S. Hunter, and D. H. Cobden, *Nature* **500**, 431 (2013).
- <sup>15</sup>S. Lysenko, V. Vikhnin, A. Rua, F. Fernandez, and H. Liu, *Phys. Rev. B* **82**, 205425 (2010).
- <sup>16</sup>A. Pashkin, C. Kübler, H. Ehrke, R. Lopez, A. Halabica, R. F. Haglund, R. Huber, and A. Leitenstorfer, *Phys. Rev. B* **83**, 195120 (2011).
- <sup>17</sup>T. L. Cocker, L. V. Titova, S. Fourmaux, G. Holloway, H.-C. Bandulet, D. Brassard, J.-C. Kieffer, M. A. El Khakani, and F. A. Hegmann, *Phys. Rev. B* **85**, 155120 (2012).
- <sup>18</sup>I. Balberg and S. Trokman, *J. Appl. Phys.* **46**, 2111 (1975).
- <sup>19</sup>O. B. Danilov and A. I. Sidorov, *Tech. Phys.* **44**, 1345 (1999).
- <sup>20</sup>P. A. Do, A. Hendaoui, E. Mortazy, M. Chaker, and A. Haché, *Opt. Commun.* **288**, 23 (2013).
- <sup>21</sup>J. D. Ryckman, V. Diez-Blanco, J. Nag, R. E. Marvel, B. K. Choi, R. F. Haglund, and S. M. Weiss, *Opt. Express* **20**, 13215 (2012).
- <sup>22</sup>J. D. Ryckman, K. A. Hallman, R. E. Marvel, R. F. Haglund, and S. M. Weiss, *Opt. Express* **21**, 10753 (2013).
- <sup>23</sup>F. Cilento, C. Giannetti, G. Ferrini, S. Dal Conte, T. Sala, G. Coslovich, M. Rini, A. Cavalleri, and F. Parmigiani, *Appl. Phys. Lett.* **96**, 021102 (2010).
- <sup>24</sup>M. A. Kats, R. Blanchard, P. Genevet, Z. Yang, M. M. Qazilbash, D. N. Basov, S. Ramanathan, and F. Capasso, *Opt. Lett.* **38**, 368 (2013).
- <sup>25</sup>Y.-G. Jeong, H. Bernien, J.-S. Kyoung, H.-R. Park, H.-S. Kim, J.-W. Choi, B.-J. Kim, H.-T. Kim, K. J. Ahn, and D.-S. Kim, *Opt. Express* **19**, 21211 (2011).
- <sup>26</sup>M. J. Dicken, K. Aydin, I. M. Pryce, L. A. Sweatlock, E. M. Boyd, S. Walavalkar, J. Ma, and H. A. Atwater, *Opt. Express* **17**, 18330 (2009).
- <sup>27</sup>M. S. Grinolds, V. A. Lobastov, J. Weissenrieder, and A. H. Zewail, *Proc. Natl. Acad. Sci. U.S.A.* **103**, 18427 (2006).
- <sup>28</sup>V. A. Lobastov, J. Weissenrieder, J. Tang, and A. H. Zewail, *Nano Lett.* **7**, 2552 (2007).
- <sup>29</sup>A. Cavalleri, Cs. Tóth, C. W. Siders, J. A. Squier, F. Raksi, P. Forget, and J. C. Kieffer, *Phys. Rev. Lett.* **87**, 237401 (2001).
- <sup>30</sup>M. Hada, K. Okimura, and J. Matsuo, *Phys. Rev. B* **82**, 153401 (2010).
- <sup>31</sup>M. Hada, K. Okimura, and J. Matsuo, *Appl. Phys. Lett.* **99**, 051903 (2011).
- <sup>32</sup>M. M. Qazilbash, A. Tripathi, A. A. Schafgans, B.-J. Kim, H.-T. Kim, Z. Cai, M. V. Holt, J. M. Maser, F. Keilmann, O. G. Shpyrko, and D. N. Basov, *Phys. Rev. B* **83**, 165108 (2011).
- <sup>33</sup>A. Barty, S. Boutet, M. J. Bogan, S. Hau-Riege, S. Marchesini, K. Sokolowski-Tinten, N. Stojanovic, R. Tobey, H. Ehrke, A. Cavalleri,

- S. Dsterer, M. Frank, S. Bajt, B. W. Woods, M. M. Seibert, J. Hajdu, R. Treusch, and H. N. Chapman, *Nat. Photonics* **2**, 415 (2008).
- <sup>34</sup>M. Eichberger, H. Schäfer, M. Krumova, M. Beyer, J. Demsar, H. Berger, G. Moriena, G. Sciaini, and R. J. D. Miller, *Nature* **468**, 799 (2010).
- <sup>35</sup>M. Borek, F. Qian, V. Nagabushnam, and R. K. Singh, *Appl. Phys. Lett.* **63**, 3288 (1993).
- <sup>36</sup>S. Lysenko, V. Vikhnin, F. Fernandez, A. Rua, and H. Liu, *Phys. Rev. B* **75**, 075109 (2007).
- <sup>37</sup>J. C. Stover, *Optical Scattering: Measurements and Analysis* (SPIE Optical Engineering Press, Bellingham, Washington, 1995).
- <sup>38</sup>V. A. Sterligov, P. Cheyssac, R. Kofman, S. I. Lysenko, P. M. Lytvyn, B. Vohnsen, S. I. Bozhevolnyi, and A. A. Maradudin, *Phys. Status Solidi B* **229**, 1283 (2002).
- <sup>39</sup>J. Elson, J. Rahn, and J. Bennett, *Appl. Opt.* **22**, 3207 (1983).
- <sup>40</sup>S. Schröder, A. Duparre, L. Coriand, A. Tünnermann, D. Penalver, and J. Harvey, *Opt. Express* **19**, 9820 (2011).
- <sup>41</sup>R. Lopez, L. C. Feldman, and R. F. Haglund, *Phys. Rev. Lett.* **93**, 177403 (2004).
- <sup>42</sup>S. Lysenko, A. Rua, F. Fernandez, and H. Liu, *J. Appl. Phys.* **105**, 043502 (2009).
- <sup>43</sup>R. Lopez, R. F. Haglund, L. C. Feldman, L. A. Boatner, and T. E. Haynes, *Appl. Phys. Lett.* **85**, 5191 (2004).
- <sup>44</sup>S. Wall, L. Foglia, D. Wegkamp, K. Appavoo, J. Nag, R. F. Haglund, J. Stähler, and M. Wolf, *Phys. Rev. B* **87**, 115126 (2013).
- <sup>45</sup>M. S. Laad, L. Craco, and E. Müller-Hartmann, "Metal-insulator transition in rutile-based VO<sub>2</sub>," *Phys. Rev. B* **73**, 195120 (2006).
- <sup>46</sup>M. Gatti, F. Bruneval, V. Olevano, and L. Reining, "Understanding correlations in vanadium dioxide from first principles," *Phys. Rev. Lett.* **99**, 266402 (2007).
- <sup>47</sup>R. A. Aliev, V. N. Andreev, V. M. Kapralova, V. A. Klimov, A. I. Sobolev, and E. B. Shadrin, *Phys. Solid State* **48**, 929 (2006).
- <sup>48</sup>A. Srivastava, T. S. Herg, S. Saha, B. Nina, A. Annadi, N. Naomi, Z. Q. Liu, S. Dhar, Ariando, J. Ding, and T. Venkatesan, *Appl. Phys. Lett.* **100**, 241907 (2012).
- <sup>49</sup>V. A. Klimov, I. O. Timofeeva, S. D. Khanin, E. B. Shadrin, A. V. Ilinskii, and F. Silva-Andrade, *Tech. Phys.* **47**, 1134 (2002).
- <sup>50</sup>J. D. Budai, A. Tselev, J. Z. Tischler, E. Strelcov, A. Kolmakov, W. J. Liu, A. Gupta, and J. Narayan, *Acta Mater.* **61**, 2751 (2013).
- <sup>51</sup>V. L. Ginzburg, A. P. Levanyuk, and A. A. Sobyenin, *Phys. Rep.* **57**, 151 (1980).